UCLA
UCLA Previously Published Works

Title

A Nitrogen- and Self-Doped Titania Coating Enables the On-Demand Release of Free Radical Species

Permalink

Journal

ISSN

Authors

Chen, Xin
Zhang, Yulong
Wu, Benjamin
et al.

Publication Date

DOI

Peer reviewed

A Nitrogen- and Self-Doped Titania Coating Enables the On-Demand Release of Free Radical Species

Xin Chen,*,[†] Yulong Zhang,[‡] Benjamin Wu,[‡,§,∥,⊥] and Gaurav Sant[†,§,∥,⊥,#]

[†]Laboratory for the Chemistry of Construction Materials (LC[2]), Department of Civil and Environmental Engineering, [‡]Departments of Bioengineering, Advanced Prosthodontics, and Orthopedic Surgery, [§]Department of Materials Science and Engineering, [∥]California Nanosystems Institute (CNSI), [⊥]Weintraub Center for Reconstructive Biotechnology, and [#]Institute for Carbon Management (ICM), University of California, Los Angeles, California 90095, United States

ABSTRACT: For potential applications such as suppressing the onset of peri-implant infections, a doped titania coating was developed to induce free radical release because of its ability for microbial elimination. The coatability of the sol−gel precursor is robust since the suspension's rheology can be modified to attain uniform and complete surface coverage. The coating is composed of a mixture of anatase and rutile polymorphs doped with nitrogen (N^{3-}), and it contains substoichiometric Ti^{2+} and Ti^{3+} species. Nitrogen doping results in a 0.4 eV band gap shift, while the defects induce photocurrent generation under visible light excitation up to 650 nm. Greater currents were observed in the nitrogen-doped titania at wavelengths above 450 nm vis-à-vis its (singularly) self-doped counterparts. The (photo)electrochemical behavior and photoactivity of the coating were evaluated by assessing redox species formation in a background aqueous solution. In the absence of any illumination, the coating behaved as an insulator and inhibited the activities of both oxidative and reductive species. On the other hand, under illumination, the coating enhances oxidation processes and inhibits reduction reactions within a near-field region wherein release of free radicals occurs and is constrained (delimited).
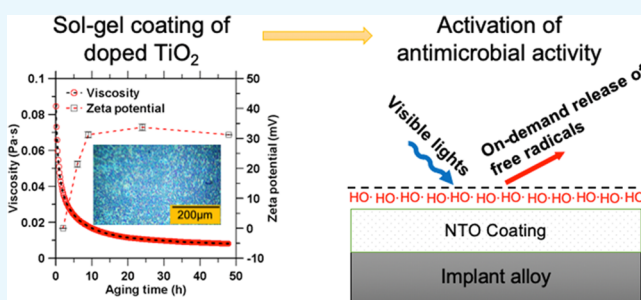
INTRODUCTION

Titanium-based alloys are ubiquitously used as dental implant materials. However, the infection of implants, an increasingly common occurrence, is problematic because of the difficulties associated with surgical intervention or (in)effective chemical treatments.[1] Recently, it has been shown that photoactive TiO_2 coatings can prevent microbial infections.[2−4] This self-cleaning (bactericidal) attribute is on account of the photoactivity displayed by TiO_2 under illumination[5]

$$h\nu + TiO_2 \rightarrow TiO_2(e^- + h^+) \tag{1}$$
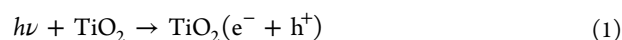
where h is Planck's constant, ν is the frequency of incident light, and e^- and h^+ are electrons and electron holes, respectively. The photoexcited e^-−h^+ pair can react with aqueous species to produce free radicals, for example, HO, O_2^-, and H_2O_2, which are detrimental to microbes.[6] As body tissues are penetrable by visible light,[7] the radical-generation ability of TiO_2 could be exploited to develop an in situ and light-activated coating for implants that would prevent infections. Importantly, the potential risks posed to body tissues following exposure to ultraviolet light and its limited penetration depth (<0.5 mm), that is, vis-à-vis visible light (0.5−10 mm),[7] create opportunities for new coatings sensitive to visible light illumination. Among all modifications, nitrogen doping[8] and self-defected species (i.e., that are formed by introducing substoichiometric Ti^{2+} and Ti^{3+} species)[9] appear most promising to impart visible light activity to TiO_2 because they do not use toxic elements that may jeopardize an implant's (bio)compatibility.

A cost-effective way to coat an implant with doped TiO_2 is via a dip-coating process using a sol−gel precursor.[10] By this method, dopants can be added to the coating precursor, and the produced coating can be designed to possess excellent photocatalytic properties and biocompatibility. However, depending on the coating conditions, the integrity of the produced coating may be diminished if cracks are to form or if only partial surface coverage is achieved.[11] The in situ treatment of an infected implant is eased if a uniformly applied coating is sensitive to visible light. In addition to the coating's uniformity, another pending concern is that free radicals (e.g., hydroxyl free radical (HO): $h^+ + H_2O \rightarrow H^+ + HO$) that are generated via the photoelectrolysis of water may not only sterilize the infected area but can also damage adjacent body tissues.[12,13]

Therefore, it is important to ensure that photocatalytically generated radical species are confined, for example, to the region in the proximate vicinity of the implant. To better understand these aspects, herein, scanning electrochemical microscopy (SECM) is used to probe the effects of free

radicals produced by the coating when it is exposed to a light source. Since free radicals are electrochemically active and can alter reduction and oxidation (redox) reaction rates, SECM detects the reactivity of redox species as a function of distance from the coating to provide insights regarding the spatial distribution of the photogenerated radicals. This allows evaluation of the effects of photostimulation in the proximate (e.g., peri-implant) region that is expected to be most affected by free radical species.

■ RESULTS AND DISCUSSION

Precursor Rheology and Coatability. In general, the coating morphologies observed are closely related to the extent of aging of the precursor. As indicated in Figure 1, the
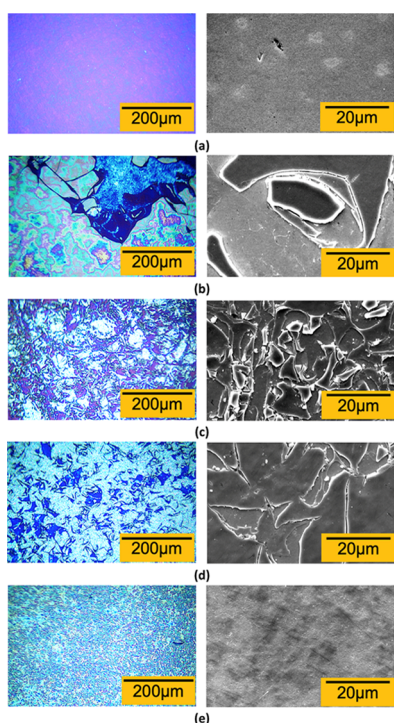
Figure 1. Representative optical (left) and SEM (right) images showing coatings formed following aging of the precursor solution for (b) 15 min, (c) 6 h, (d) 24 h, and (e) 48 h. (a) Surface of a control sample exposed to the same heat treatment as the coatings.

uncoated areas exhibit dark blue and purple regions resembling the control surface while the coated areas show interference patterns of visible light indicative of a transparent coating. Unsurprisingly, large cracks and uncoated areas persisted in coatings wherein the precursor was aged for less than 48 h. But with prolonged aging, surface coverage greatly improved such that, following 48 h of aging, superior coating attributes were observed. For example, as shown in Figure 1e, following 48 h of aging, a uniform and crack-free coating was formed.

The precursor solution's properties evolve during aging resulting in improved coatability. For example, as seen in Figure 2, the highest viscosity of 85 mPa·s was attained after the two precursor solutions are initially titrated. During aging, while stirring at a constant rate, the viscosity decreased to 9 mPa·s after 48 h. The high initial viscosity is on account of the consumption of the viscous titanium(IV) isopropoxide resulting in the formation of a polymerized gel network containing Ti^{4+} ions. However, the ζ potential of the gel
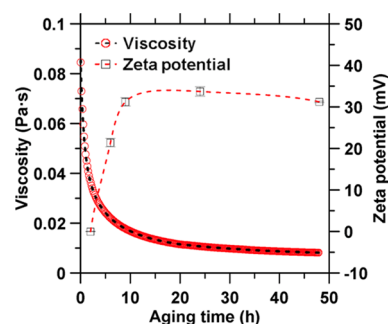
Figure 2. Viscosity evolution of the precursor solution and the ζ potential of the gel-agglomerates with increasing aging.

particles increased from near neutral charge until it saturated at a positive potential around 30 mV. The positive surface potential results in electrostatic repulsion of the gel particles away from each other. As a result, the system's viscosity decreased progressively with aging.

Phase Composition. The thickness and composition of the coating formed following aging of the precursor solution for 48 h ("48 h NTO coating") were characterized using SEM-EDS. In general, the 48 h NTO coating is 4 μm thick (Figure 3a) and contains titania with 12 ± 2 mass % nitrogen. The
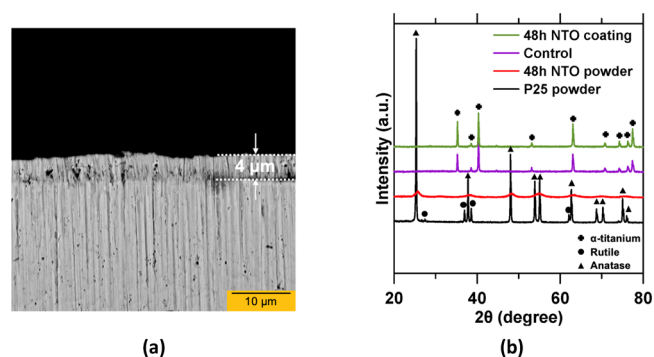

Figure 3. (a) Backscattered electron (BSE) image showing the thickness of the coating formed following aging of the precursor solution for 48 h (i.e., the 48 h NTO coating). (b) X-ray diffraction patterns of the 48 h NTO coating, the control surface, 48 h NTO powder, and the P25 powder.

lattice structure of the 48 h NTO coating and the control surfaces were characterized using X-ray diffraction (XRD). The diffraction patterns (Figure 3b) only show diffraction peaks associated with the substrate (α-titanium) but display no response from the coating or the thermal oxidation layers. In contrast, the P25 powder exhibits clear diffraction peaks mainly of anatase and trace amount of rutile; meanwhile, the powder synthesized using the 48 h aged sol−gel precursor ("48 h NTO powder") exhibits only anatase's pattern. The peak broadening observed for the 48 h NTO powder as compared to the sharp peaks displayed in the P25 pattern implies reduced ordering/crystallinity in the former case. The 48 h NTO coating itself too is expected to feature the same low crystallinity. Thus, on account of the small thicknesses of the coated (around 4 μm; see Figure 3a) and the thermal (less than 100 nm[14]) oxidation layers, Raman spectroscopy was used to acquire detailed phase compositions.

Raman spectroscopy enabled clear differentiation of the different titania phases that formed on coated surfaces, as

opposed to the thermal oxidation film that formed on uncoated, exposed regions. For example, simple thermal oxidation of the Ti-0.2%Pd alloy produced rutile-structured titania (Figure 4a) that features peaks at Raman shifts of 247,
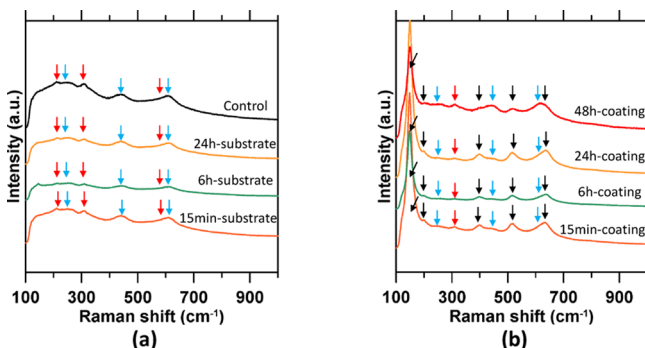
Figure 4. Representative Raman spectra obtained for (a) thermal oxides grown on uncoated exposed substrates and (b) coated surfaces. The peaks at (i) 210, 307, and 568 cm^{-1} indicate TiN[16] (denoted by red arrows), (ii) 247, 438, and 607 cm^{-1} indicate rutile (blue arrows), and (iii) 148, 199, 396, 516, and 635 cm^{-1} indicate anatase (black arrows).[15]

438, and 607 cm^{-1}.[15] The presence of TiN that features peaks at 210, 307, and 568 cm^{-1}[16] suggests its formation during the heat treatment. Importantly, no carbide residues were detected indicating that any solvents used were fully evaporated during synthesis. The Raman spectra of the coated surfaces (Figure 4b) show predominantly anatase peaks at 148, 199, 396, 516, and 635 cm^{-1}.[15] However and significantly, the Raman spectrum of the 48 h aged coating features strong peaks suggesting the presence of intermixed anatase and rutile polymorphs, which are present in similar abundance. The

presence of rutile on uncoated (thermally treated) surfaces is expected as it is the more thermally stable phase.[17] Anatase, on the other hand, is typically produced by sol−gel processing or anodizing Ti-alloys and subsequently annealing them at relatively low temperatures (e.g., below 500 °C).[18] However, if the annealing temperature exceeds 450 °C, a thin layer of rutile may form between the anatase coating and the substrate explaining the indication of both oxides in the Raman spectra (see Figure 3b).[19] The formation of the intermediate rutile layer, which often features a higher electrical resistance and corrosion resistance, is complemented by the outer anatase layer, which favors osseointegration (i.e., bone integration).[20] Most importantly, mixed-phase titania consisting of both anatase and rutile is well known to offer superior photocatalytic performance vis-à-vis single phase compositions.[21]

In addition to phase composition, light absorption depends on band structures and how they may be modified by dopants.[18] The chemical and valence information of elements contained in the thermal and coated oxides as analyzed by XPS is shown in Figure 5 and Table 1. Based on the Ti 2p spectra,

Table 1. Elemental Species and Compositions Ascertained by Quantitative XPS Analyses

surface	Ti cations (at. %)			O anions (at. %)	
	Ti^{4+}	Ti^{3+}	Ti^{2+}	lattice O	OH/defect O
control surface	52.4	36.7	10.9	67.9	32.1
48 h aged coating	54.2	33.4	12.4	66.3	33.7

the calcination process induced the formation of lower valence ("substoichiometric") titanium species, Ti^{2+} and Ti^{3+}, in the coating (Figure 5d) through a process resembling the thermal oxidation of the control surface (Figure 5a). This oxidation process is governed by the diffusion of cation interstitials and
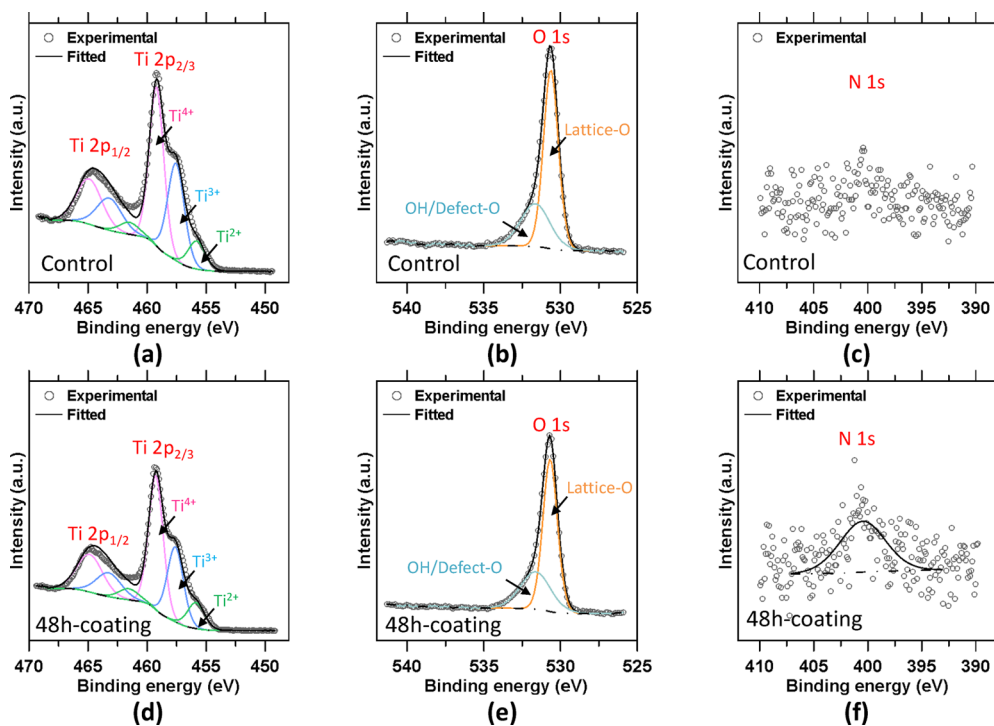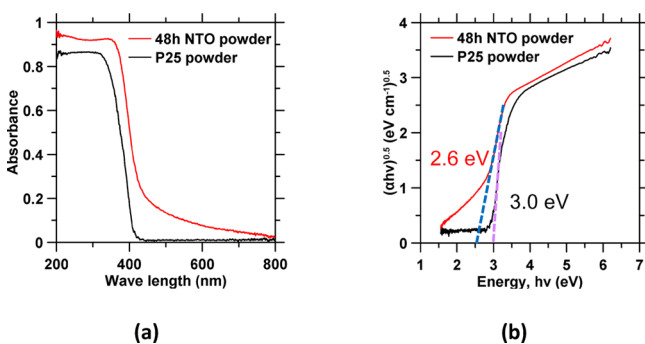

Figure 5. Representative (a,d) Ti 2p, (b,e) O 1s, and (c,f) N 1s XPS spectra acquired for the control (uncoated) sample (a−c) and the sample with the 48 h NTO coating (d−f).

anion vacancies in accordance with the point defect model.[22] When the rate of generation of cation interstitials at the substrate/coating interface is greater than the annihilation rate of stoichiometric anion vacancies at the coating/air interface, excessive interstitials will form in oxide compounds in the form of Ti^{2+} and Ti^{3+} species. These lower valence (substoichiometric) Ti ions exist in the form of point defects and also cause the surrounding O ions to be detected as defect-O (Figure 5b,e). The significant concentrations of Ti^{2+} and Ti^{3+} dopants in the coating (see Table 1) suggest that the coating is diffusion-bonded with the substrate.

Nitrogen was added to the coating precursor to serve as a dopant to extend the photoactivity of titania into the visible light range. First, expectedly, the N 1s spectrum from the control surface (Figure 5c) shows no established peak, suggesting that the nitrogen content of the thermal oxide is insignificant. However, since nitrogen is added to the coating precursor, the N 1s photoelectron peak of the coating (Figure 5f) shows a notable peak confirming that the coating not only is self-doped but is also nitrogen-doped. This nature of mixed doping results in interstitial band structures that enhance the absorption of visible light with longer wavelengths as has been highlighted previously.[23]
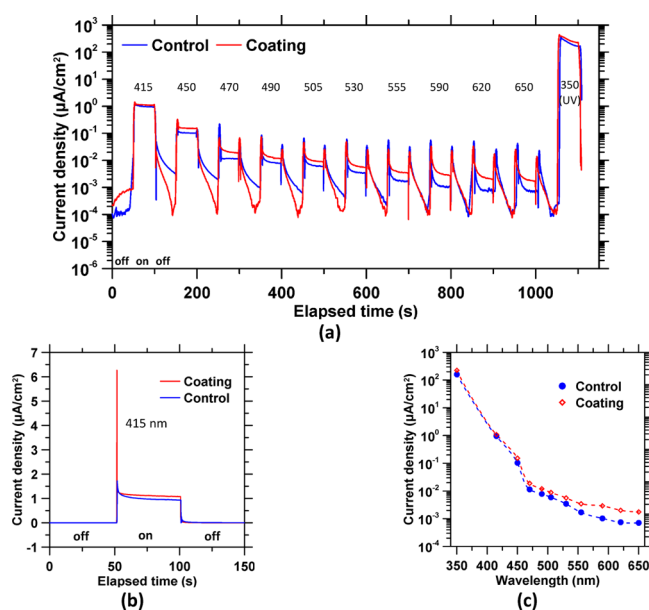
UV−vis Absorbance and Photocurrent Measurements. The photoactivity enhancements of titania resulting from the nitrogen doping was investigated by comparing the UV−vis absorbances of the 48 h NTO and the P25 powders. The UV−vis absorption spectra (Figure 6a) signify a clear

Figure 7. (a) Photocurrent responses of the uncoated alloy substrate and the substrate provisioned with the 48 h aged coating as a function of time following periodic illumination. (b) Detailed photocurrent profiles of the substrates illuminated under the 415 nm (purple) light. (c) The steady-state photocurrent density as a function of the wavelength of illumination.

Figure 6. (a) UV−vis absorbance spectra of the nitrogen doped (48 h NTO) and the undoped (P25) powders. (b) Tauc plots showing that the band gap energies for the N-doped and P25 titania powders are 2.6 and 3.0 eV, respectively.

enhancement in visible light (wavelength > 380 nm) absorption on account of nitrogen doping. The band gap energies of the powders were analyzed by converting the absorbance spectra to the Tauc plot[24] with the photon energy, $h\nu$, shown on the x axis and $(\alpha h\nu)^{0.5}$ on the y axis, where α is the absorbance coefficient, h is Planck's constant, and ν is the photon's frequency. As indicated Figure 6b, the 48 h NTO powder shows a band gap energy that is around 0.4 eV lower than the P25 powder, as expected because of its nitrogen doping[18] and lower crystallinity.[25]

To evaluate the photocatalytic behavior of the coating, photocurrents were measured in a DPBS solution while the surfaces were held at 0 $V_{Ag/AgCl}$, that is, a potential close to the open circuit potentials. Figure 7a shows the photocurrent responses of both uncoated and coated surfaces during illumination. The photocurrent profile during a single "off−on−off" cycle is shown in Figure 7b. The current spikes

following photoexcitation signify the fast generation of $e^−–h^+$ pairs, and the subsequent recombination of $e^−–h^+$ pairs resulted in the current decay until a steady-state current was attained.[26] Expectedly, significant photocurrents were generated from both the coated and uncoated samples up on illumination by blue light ($\lambda = 450$ nm) since both of these surfaces contain oxides that are self-doped with Ti^{2+} and Ti^{3+} species. The coated sample show higher spike and steady-state currents at wavelengths less than 450 nm. At greater wavelengths, both surfaces show diminished steady-state currents below 20 nA/cm²; however, the photocurrents measured from the coated surface are consistently higher than the uncoated surface due to its nitrogen doping.

The evolved photocurrent is a direct measure of the rate of generation of free radicals. The hydroxyl radical, HO·, is the most reactive among all free radicals, and its spatial distribution and effects on charge-transfer reactions were evaluated using SECM. The redox mediators used include FcMeOH and $Ru(NH_3)_6Cl_3$ that can undergo oxidation and reduction reactions at the Pt UME with applied potential:

$$Fc \rightarrow Fc^+ + e^- \qquad (2)$$

$$Ru(NH_3)_6^{3+} + e^- \rightarrow Ru(NH_3)_6^{2+} \qquad (3)$$
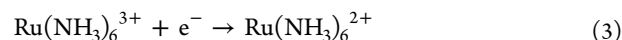
Since these reactions are one-step redox reactions, the redox current that was measured directly reveals the influence and extent of generation of HO· radicals. First, the surface reactivity of the 48 h aged coating, without illumination, was assessed by the SECM approach curves. Herein, the Pt UME was potentiostatically held at +0.4 and −0.4 $V_{Ag/AgCl}$ in DPBS solutions containing 2 mM FcMeOH and $Ru(NH_3)_6Cl_3$, respectively, so that diffusion-limiting currents are achieved. The evolution of diffusion-limiting currents was measured, while the Pt UME progressively approached the 48 h aged coating at a rate of 1 μm/s (see Figure 8a). The dashed line
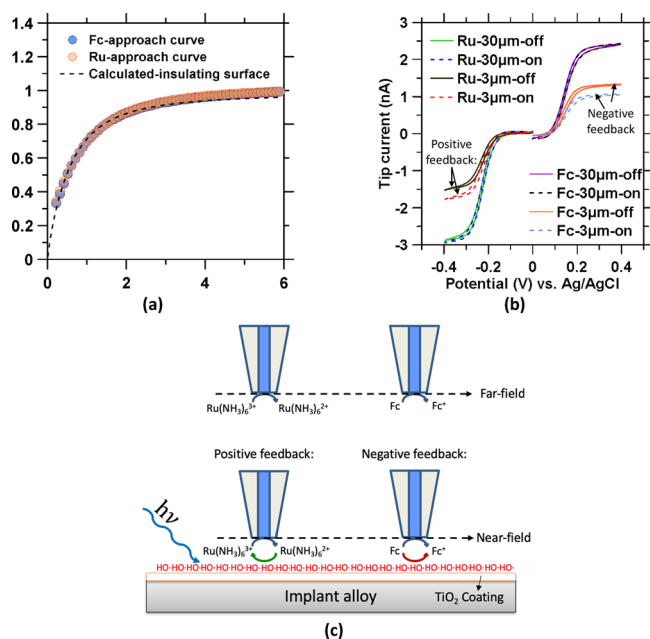
Figure 8. (a) Approach curves obtained in DPBS + 2 mM FcMeOH (denoted as Fc) and DPBS + 2 mM Ru(NH$_3$)$_6$Cl$_3$ (denoted as Ru) solutions under nonilluminated conditions. The current and distance from the substrate are normalized by the limiting currents and the tip radius. The dashed line represents the theoretical approach curve for an insulating surface. (b) Cyclic voltammetry curves conducted with the Pt UME at 3 and 30 μm away from the coating surface. "on" and "off" represent conditions with and without illumination, respectively. (c) A schematic illustrating the mechanism of positive and negative feedbacks.

shows the calculated response,[27] representing the theoretical approach curve of an insulating substrate. A good match between the measured curves and the calculated curve indicates that, when not excited by light, the coating inhibits both oxidative and reductive charge-transfer reactions. In other words, the coating is expected to provide excellent corrosion resistance to the implant ensuring enhanced chemical durability.

The diffusion-limiting current measured at Pt UME is subject to feedback effects from the substrate if HO$^\cdot$ radicals are generated by the coating up on its illumination. Based on the current−distance relationship established by the approach curves, the Pt UME was positioned 3 and 30 μm above the coating surface, and cyclic voltammetry (CV) was used to probe feedback effects. As shown in Figure 8b, when the Pt UME is placed 3 μm above the coating in the Ru-DPBS solution, the limiting current of the reduction reaction, that is, the plateau current associated with reducing Ru(NH$_3$)$_6^{3+}$ to Ru(NH$_3$)$_6^{2+}$, increases under UV−vis illumination. This indicates that the coating's surface enhances the oxidation reaction so that more oxidized Ru(NH$_3$)$_6^{3+}$ can flow to the tip where it is subsequently reduced. However, the limiting current decreases for the tip-oxidation reaction (Fc to Fc$^+$) under the same conditions, indicating that surface reduction is inhibited and the Fc concentration at the tip is reduced. As such, the coating exhibits positive feedback following the UME's reduction but offers negative feedback for UME-oxidation reactions. On the other hand, feedback effects are both negligible when the Pt UME is positioned 30 μm above

the coating, that is, when no reaction effects associated with the substrate are detected by the UME.

To better illustrate the feedback effect, Figure 8c shows UME-substrate interactions. When excited by light, free hydroxyl radicals (HO$^\cdot$) are produced and are adsorbed at the coating surface.[28] When reducing Ru(NH$_3$)$_6^{3+}$ to Ru-(NH$_3$)$_6^{2+}$ at the Pt UME, the produced Ru(NH$_3$)$_6^{2+}$ diffuses toward the substrate and reacts with the HO$^\cdot$ radicals to form Ru(NH$_3$)$_6^{3+}$, which diffuses back toward the UME. Therefore, a UME-reduction, substrate-oxidation loop is set up, and the substrate elevates the concentration of Ru(NH$_3$)$_6^{3+}$ that promotes tip-reduction, that is, providing positive feedback. In the case of UME-oxidation of Fc to Fc$^+$, Fc is not only oxidized at the Pt UME due to the applied potential but also at the substrate due to photoinduced HO$^\cdot$ radicals such that the substrate competes with the UME resulting in negative feedback. In any event, the changes observed in limiting currents (Figure 8b) signify that, upon illumination, the coating can enhance oxidation and inhibit reduction reactions by nearly 20% within a near-field region (i.e., on the order of around 3 μm from the substrate) in solution. This is attributed to the high activity of free radicals (e.g., HO$^\cdot$) affecting redox rates of the mediators in this region. As the distance from the coating surface increases, the concentration of free radicals reduces significantly as these species are consumed or decomposed. As a result, the CV curves acquired at 30 μm show limiting currents for both redox reactions that are no longer affected by illumination, indicative of a negligible free radical activity. Taken together, these results suggest that coating materials of the nature developed herein are well-suited for localized free radical release in close vicinity to implant and tissue surfaces.

■ SUMMARY AND CONCLUSIONS

A defected titania composition was synthesized for potential applications such as coating of implant (titanium alloy) surfaces. The coatability of the sol−gel precursor was found to increase with increasing aging on account of the development of electrostatic repulsion among colloidal charged particulates in solution. As a result, coatings aged for 48 h exhibited complete surface coverage and uniformity and hence superior coatability. Careful analysis using Raman spectroscopy identified that the coating is composed of intermixed anatase/rutile components that are clearly distinguished from the typical thermal oxides that form following heat treatment in air. Indeed, XPS indicates that the coating is not only doped with nitrogen but also self-defected and therefore features substoichiometric Ti^{2+} and Ti^{3+} species. These defects promote visible light absorption of the coating by alteration of the band structure. Upon illumination, SECM detects the formation and release of oxidative hydroxyl radicals within a proximate region on the order of several micrometers. Therefore and significantly, this coating may be appropriate to address clinical issues such as the onset of localized peri-implant infections due to the formation of bactericidal hydroxyl radicals while minimizing the exposure impacts on adjacent body tissues. Expectedly, an important follow-up step in the development of such materials requires explicit analysis of their antimicrobial activity, as well as cytological compatibility, to ensure that they are suitable for use with practical hard tissue implants.

MATERIALS AND METHODS

Sample Preparation. The external implant surface was modified by applying a coating precursor. Briefly, a sol−gel Solution A was prepared by mixing 500 μL of titanium(IV) isopropoxide (Ti[OCH(CH$_3$)$_2$]$_4$), 6 mL of ethanol, 70 μL of 70% HNO$_3$, and 10 mg of sodium dodecyl sulfate (CH$_3$(CH$_2$)$_{11}$SO$_4$Na) using vortex mixing until a clear solution was obtained. Next, nitrogen doping was effected by preparation of sol−gel Solution B, which involved mixing 4.4 mL of DI water, 1.2 mL of 100% ethanol, and 183 μL of a 15% ammonium bicarbonate (NH$_4$HCO$_3$) solution. The precursor was then composed by titrating Solution B into Solution A dropwise while stirring. Thereafter, the precursor was aged at room temperature while stirring. During aging, the rheology of the precursor was characterized (TA Discovery) using a vane-cup assembly at a constant rotation speed of 100 rad/s. The measured torque was used to quantify the solution's viscosity. In addition, the ζ potential of the precursor (Malvern Zetasizer), during aging, was measured using samples diluted with DI water (volume ratio 1:200).

Since trace dosages of Pd in TiO$_2$ can enhance photocatalytic activity,[29,30] Grade 7 Ti discs (Ti-0.2%Pd, 7 mm: diameter, 1.5 mm: thickness) were selected as the substrate. The discs were progressively polished to a 0.05 μm surface finish using colloidal silica and sequentially sonicated in acetone and DI water for 10 min each. Thereafter, the discs were dip-coated with the precursor and aged for 15 min, 6 h, 12 h, 24 h, and 48 h. The dipping operation was controlled by a robotic dispenser that permits a constant withdrawal rate of 0.3 mm/s. The coated discs were dried in a fume hood for 10 min and then cured in an oven at 150 °C for 30 min. These dip-coating and heating processes were successively repeated four times. The coated samples were subsequently heated in air (heating rate: 1 °C/min) to 450 °C. The samples were held at this temperature for 2 h to remove residual solvents and to facilitate phase conversion(s). An uncoated "control" substrate underwent identical heat treatments to enable the formation of an oxidation layer on its exposed surfaces. Along with the coated substrates, the 48 h aged sol−gel precursor was heated in a glass Petri dish using the same procedure to produce the nitrogen-doped TiO$_2$ powder (48 h NTO powder). A standard P25 TiO$_2$ powder (Sigma Aldrich Aeroxide) representing the undoped TiO$_2$ was used as a comparison to the doped NTO powder.

Phase Composition Characterization. Microstructural and phase analyses of the NTO powders and the coatings were carried out using X-ray diffraction (XRD: Panalytical X'Pert Pro) and Raman spectroscopy (Renishaw inVia, using a 633 nm laser source). The morphology and composition of the processed surfaces were characterized using scanning electron microscopy (SEM, FEI NOVA 230) coupled with an energy dispersive X-ray emission spectrometer (EDS, Thermo Scientific UltraDry). Finally, both elemental compositions and valence states were examined by X-ray photoelectron spectroscopy (XPS, Kratos Ultra DLD) using monochromated Al Kα radiation (15 kV, 10 mA), with a pass energy of 20 eV for high-resolution surveys. It should be noted that, prior to the XPS analysis, the sample surfaces were cleaned by Ar$^+$ sputtering for 3 min to remove any surface impurities. Following XPS analysis, quantitative analysis of the spectra was carried out using the CasaXPS software.[31]

Photocatalysis Characterization. UV−vis absorbances of the 48 h NTO and the P25 powders were determined using diffuse reflectance spectroscopy (SHIMADZU UV-3101PC). To characterize the photocatalytic properties of the coated surfaces, photocurrent measurements were conducted using a potentiostat (Princeton Applied Research: VersaSTAT 4) that employs a Pt counter electrode and a Ag/AgCl reference electrode. Dulbecco's phosphate-buffered saline (DPBS, pH 7.4) was used as an electrolyte with an ion concentration and isotonic osmolarity analogous to human blood. During the electrochemical analysis, illumination was provided using a xenon lamp (Rofin PL 500) with tunable output wavelengths spanning from 350 to 650 nm. A constant illumination intensity of 20 mW/cm^2 over 50 s cycles of illumination was applied for both ultraviolet and visible wavelengths of light. The effects of photocatalytic redox reactions occurring at the coating/solution interface were evaluated using scanning electrochemical microscopy (SECM: HEKA ElProScan) operated in feedback mode. A 3.3 mW/cm^2 white light was used as the light source in SECM measurements. The SECM is equipped with a 10 μm radius Pt ultra-microelectrode (UME) with an RG ratio, that is, the ratio of the glass sheath radius to the Pt UME radius, of 2.4. The DPBS solution is used as the background electrolyte with 2 mM ferrocenemethanol (FcMeOH, C$_{11}$H$_{12}$FeO) and hexaammineruthenium chloride (Ru(NH$_3$)$_6$Cl$_3$) as the oxidative and reductive redox mediators, respectively.

AUTHOR INFORMATION

Corresponding Author
*E-mail: xinchen0601@ucla.edu.

ORCID
Xin Chen: 0000-0003-3273-4431
Yulong Zhang: 0000-0003-3089-196X
Gaurav Sant: 0000-0002-1124-5498

Notes
The authors declare no competing financial interest.
The analysis scripts and data sets generated during and/or analyzed over the course of the title study are available from the corresponding author upon reasonable request.

REFERENCES

(1) Berglundh, T.; Jepsen, S.; Stadlinger, B.; Terheyden, H. Peri-implantitis and Its Prevention. *Clin. Oral Implants Res.* **2019**, 150.
(2) Simchi, A.; Tamjid, E.; Pishbin, F.; Boccaccini, A. R. Recent Progress in Inorganic and Composite Coatings with Bactericidal Capability for Orthopaedic Applications. *Nanomed.: Nanotechnol. Biol. Med.* **2011**, 7, 22−39.

(3) Shiraishi, K.; Koseki, H.; Tsurumoto, T.; Baba, K.; Naito, M.; Nakayama, K.; Shindo, H. Antibacterial Metal Implant with a TiO2-conferred Photocatalytic Bactericidal Effect against Staphylococcus Aureus. *Surf. Interface Anal Int. J. Devoted Dev. Appl. Tech. Anal. Surf. Interfaces Thin Films* **2009**, *41*, 17−22.

(4) Suketa, N.; Sawase, T.; Kitaura, H.; Naito, M.; Baba, K.; Nakayama, K.; Wennerberg, A.; Atsuta, M. An Antibacterial Surface on Dental Implants, Based on the Photocatalytic Bactericidal Effect. *Clin. Implant Dent. Relat. Res.* **2005**, *7*, 105−111.

(5) Fujishima, A.; Honda, K. Electrochemical Photolysis of Water at a Semiconductor Electrode. *Nature* **1972**, *238*, 37.

(6) Kühn, K. P.; Chaberny, I. F.; Massholder, K.; Stickler, M.; Benz, V. W.; Sonntag, H.-G.; Erdinger, L. Disinfection of Surfaces by Photocatalytic Oxidation with Titanium Dioxide and UVA Light. *Chemosphere* **2003**, *53*, 71−77.

(7) Keereweer, S.; Van Driel, P. B. A. A.; Snoeks, T. J. A.; Kerrebijn, J. D. F.; de Jong, R. J. B.; Vahrmeijer, A. L.; Sterenborg, H. J. C. M.; Löwik, C. W. G. M. Optical Image-Guided Cancer Surgery: Challenges and Limitations. *Clin. Cancer Res.* **2013**, *19*, 3745−3754.

(8) Asahi, R.; Morikawa, T.; Ohwaki, T.; Aoki, K.; Taga, Y. Visible-Light Photocatalysis in Nitrogen-Doped Titanium Oxides. *Science* **2001**, *293*, 269−271.

(9) Justicia, I.; Ordejón, P.; Canto, G.; Mozos, J. L.; Fraxedas, J.; Battiston, G. A.; Gerbasi, R.; Figueras, A. Designed Self-doped Titanium Oxide Thin Films for Efficient Visible-light Photocatalysis. *Adv. Mater.* **2002**, *14*, 1399−1402.

(10) Yun, H.; Li, J.; Chen, H.-B.; Lin, C.-J. A Study on the N-, S-and Cl-Modified Nano-TiO2 Coatings for Corrosion Protection of Stainless Steel. *Electrochim. Acta* **2007**, *52*, 6679−6685.

(11) Bockmeyer, M.; Löbmann, P. Crack Formation in TiO_2 Films Prepared by Sol−Gel Processing: Quantification and Characterization. *Thin Solid Films* **2007**, *515*, 5212−5219.

(12) Halliwell, B. Free Radicals and Antioxidants: A Personal View. *Nutr. Rev.* **1994**, *52*, 253−265.

(13) Turchi, C. S.; Ollis, D. F. Photocatalytic Degradation of Organic Water Contaminants: Mechanisms Involving Hydroxyl Radical Attack. *J. Catal.* **1990**, *122*, 178−192.

(14) Wang, G.; Li, J.; Lv, K.; Zhang, W.; Ding, X.; Yang, G.; Liu, X.; Jiang, X. Surface Thermal Oxidation on Titanium Implants to Enhance Osteogenic Activity and in Vivo Osseointegration. *Sci. Rep.* **2016**, *6*, 31769.

(15) Lubas, M.; Jasinski, J. J.; Sitarz, M.; Kurpaska, L.; Podsiad, P.; Jasinski, J. Raman Spectroscopy of TiO_2 Thin Films Formed by Hybrid Treatment for Biomedical Applications. *Spectrochim. Acta, Part A* **2014**, *133*, 867−871.

(16) de Sousa, R. R. M.; Sato, P. S.; Viana, B. C.; Alves, C., Jr.; Nishimoto, A.; Nascente, P. A. P. Cathodic Cage Plasma Deposition of TiN and TiO_2 Thin Films on Silicon Substrates. *J. Vac. Sci. Technol., A* **2015**, *33*, No. 041502.

(17) Ting, C.-C.; Chen, S.-Y.; Liu, D.-M. Structural Evolution and Optical Properties of TiO_2 Thin Films Prepared by Thermal Oxidation of Sputtered Ti Films. *J. Appl. Phys.* **2000**, *88*, 4628−4633.

(18) Paramasivam, I.; Jha, H.; Liu, N.; Schmuki, P. A Review of Photocatalysis Using Self-organized TiO_2 Nanotubes and Other Ordered Oxide Nanostructures. *Small* **2012**, *8*, 3073−3103.

(19) Tighineanu, A.; Albu, S. P.; Schmuki, P. Conductivity of Anodic TiO_2 Nanotubes: Influence of Annealing Conditions. *Phys. Status Solidi RRL* **2014**, *8*, 158−162.

(20) Rohanizadeh, R.; Al-Sadeq, M.; LeGeros, R. Z. Preparation of Different Forms of Titanium Oxide on Titanium Surface: Effects on Apatite Deposition. *J. Biomed. Mater. Res. Part Off. J. Soc. Biomater. Jpn. Soc. Biomater. Aust. Soc. Biomater. Korean Soc. Biomater.* **2004**, *71A*, 343−352.

(21) Ohno, T.; Tokieda, K.; Higashida, S.; Matsumura, M. Synergism between Rutile and Anatase TiO_2 Particles in Photocatalytic Oxidation of Naphthalene. *Appl. Catal., A* **2003**, *244*, 383−391.

(22) Macdonald, D. D. The Point Defect Model for the Passive State. *J. Electrochem. Soc.* **1992**, *139*, 3434−3449.

(23) Liu, M.; Qiu, X.; Miyauchi, M.; Hashimoto, K. Cu (II) Oxide Amorphous Nanoclusters Grafted Ti^{3+} Self-Doped TiO_2: An Efficient Visible Light Photocatalyst. *Chem. Mater.* **2011**, *23*, 5282−5286.

(24) Tauc, J. Optical Properties and Electronic Structure of Amorphous Ge and Si. *Mater. Res. Bull.* **1968**, *3*, 37−46.

(25) Zhu, L.; Lu, Q.; Lv, L.; Wang, Y.; Hu, Y.; Deng, Z.; Lou, Z.; Hou, Y.; Teng, F. Ligand-Free Rutile and Anatase TiO 2 Nanocrystals as Electron Extraction Layers for High Performance Inverted Polymer Solar Cells. *RSC Adv.* **2017**, *7*, 20084−20092.

(26) Dai, Y.; Sun, Y.; Yao, J.; Ling, D.; Wang, Y.; Long, H.; Wang, X.; Lin, B.; Zeng, T. H.; Sun, Y. Graphene-Wrapped TiO_2 Nanofibers with Effective Interfacial Coupling as Ultrafast Electron Transfer Bridges in Novel Photoanodes. *J. Mater. Chem. A* **2014**, *2*, 1060−1067.

(27) Wei, C.; Bard, A. J.; Mirkin, M. V. Scanning Electrochemical Microscopy. 31. Application of SECM to the Study of Charge Transfer Processes at the Liquid/Liquid Interface. *J. Phys. Chem.* **1995**, *99*, 16033−16042.

(28) Park, H. S.; Leonard, K. C.; Bard, A. J. Surface Interrogation Scanning Electrochemical Microscopy (SI-SECM) of Photoelectrochemistry at a W/Mo-BiVO4 Semiconductor Electrode: Quantification of Hydroxyl Radicals during Water Oxidation. *J. Phys. Chem. C* **2013**, *117*, 12093−12102.

(29) Allam, N. K.; Poncheri, A. J.; El-Sayed, M. A. Vertically Oriented Ti−Pd Mixed Oxynitride Nanotube Arrays for Enhanced Photoelectrochemical Water Splitting. *ACS Nano* **2011**, *5*, 5056−5066.

(30) Li, Q.; Li, Y. W.; Wu, P.; Xie, R.; Shang, J. K. Palladium Oxide Nanoparticles on Nitrogen-Doped Titanium Oxide: Accelerated Photocatalytic Disinfection and Post-Illumination Catalytic "Memory". *Adv. Mater.* **2008**, *20*, 3717−3723.

(31) Fairley, N. *CasaXPS VAMAS Processing Software; Available World Wide Web Httpwww Casaxps Com* 2010.